

Data-Driven Selection of Actuators for Optimal Control of Airfoil Separation

Debraj Bhattacharjee, Bjoern Klose,
Gustaaf B. Jacobs, and Maziar S. Hemati

Received date and accepted date

Abstract We present a systematic approach for determining the optimal actuator location for separation control from input-output response data, gathered from numerical simulations or physical experiments. The Eigensystem Realization Algorithm is used to extract state-space descriptions from the response data associated with a candidate set of actuator locations. These system realizations are then used to determine the actuator location among the set that can drive the system output to an arbitrary value with minimal control effort. The solution of the corresponding minimum energy optimal control problem is evaluated by computing the generalized output controllability Gramian. We use the method to analyze high-fidelity numerical simulation data of the

D. Bhattacharjee

Electrical and Computer Engineering, University of Minnesota, Minneapolis, MN 55455

B. Klose and G.B. Jacobs

Aerospace Engineering, San Diego State University, San Diego, CA 92182

M. S. Hemati

Aerospace Engineering and Mechanics, University of Minnesota, Minneapolis, MN 55455

Tel.: +612-625-6857

Fax: +612-626-1558

E-mail: mhemati@umn.edu

lift and separation-angle responses to a pulse of localized body-force actuation from six distinct locations on the upper surface of a NACA 65(1)-412 airfoil. We find that the optimal location for controlling lift is different from the optimal location for controlling separation angle. In order to explain the physical mechanisms underlying these differences, we conduct controllability analyses of the flowfield by leveraging the dynamic mode decomposition with control algorithm. These modal analyses of flowfield response data reveal that excitation of coherent structures in the wake benefit lift control; whereas, excitation of coherent structures in the shear layer benefit separation-angle control.

1 Introduction

Flow separation can degrade performance in many engineering systems, through reduced lift, increased drag, and decreased efficiency. To alleviate the effects of flow separation on aerodynamic performance, active flow control has been considered since the inception of the field of aerodynamics [1, 2].

Open-loop flow control strategies based on various actuator technologies [3]—such as plasma actuators [4–6], fluidic oscillators [7–11], and synthetic jets [12–16]—have been shown to effectively alter separated flows, and in some cases to even yield complete reattachment. In [17], oscillatory forcing was found to improve control authority for separation control. Several studies have observed that actuating at the dominant shear layer frequency is effective for mitigating flow separation [18–21]. Other studies have reported that separation mitigation is most effective when actuation is applied at the separation bubble frequency, not the shear layer frequency [22]. Further, it was shown that nonlinear flow interactions can result in lock-on effects that influence the optimal forcing frequency [23, 24].

Recent investigations have sought to identify candidate actuation frequencies more objectively using operator-based and data-driven modal analysis techniques—such as linear stability analysis, resolvent analysis, and dynamic mode decomposition (DMD) [14, 20, 25–28]. Actuation designed based on these analyses yielded improved open-loop controller designs; however, the actuator positions considered were fixed and may not necessarily translate to the optimal performance achievable in terms of separation control.

The positioning of actuators and sensors is known to play a central role in determining achievable control performance. In most scenarios, using all available actuators and sensors will yield the highest performance for a given system. However, through judicious selection and placement, it is possible to achieve optimal control performance using fewer actuators and sensors. To this end, systems theoretic optimization approaches for sensor and actuator placement have been proposed in a number of studies. The effect of white noise disturbances on actuator and sensor placement for the Ginzburg-Landau system was investigated in [29], where numerical optimization was used to minimize the actuator effort and perturbation magnitude in an \mathcal{H}_2 sense. In [30], a branch-and-bound procedure was proposed to determine the optimal actuator placement with constraints on the number of actuators. Further, sensor selection for flow reconstruction has been considered in [31, 32], and for feedback flow control in [33].

Despite all of these advances, the optimal selection problem has remained relatively unexplored within the context of separation control. Placing the actuators in locations that are intuitively optimal [34, 35] may not be optimal for control performance. Therefore, the selection from a set of candidate locations using systematic criteria may assist in identifying the actuator location with the highest performance index. Further, such an approach would ensure that the resulting selection would be feasible in practice—as the candidate set

would be constructed to adhere to physical and economic constraints on the type and placement of actuators.

In separation control, actuator placement is usually strongly correlated with the location of the separation point. In steady flows, this location of flow separation from a no-slip wall is well-known to be identified exactly by Prandtl's condition for separation in the Eulerian frame, through a point of zero skin friction and a negative friction gradient in the wall-tangential direction. However, flow separation from a no-slip wall can also be considered in the Lagrangian frame by understanding fluid tracers breaking away from a wall. While much work has been done on unsteady separation (see [36]), only recently was it shown that the dynamics of unsteady flow separation are better analyzed in a Lagrangian frame, wherein the Lagrangian separation point is fixed for a periodic flow [37]. In [37], it was shown that the time-dependent *separation angle* $\theta(t)$ of the Lagrangian unstable manifold can be computed using pressure and skin-friction data. In [37] and [38], it was further shown that particles near a separation point are drawn towards an unstable manifold—i.e, an attracting line in the flowfield.

In [39], the separation angle and lift response was recorded to a flow pulse at six candidate actuator locations. It was demonstrated that an increase in separation angle leads the separation line to become concave, for any location upstream of the separation point. In turn, the concavity of the separation line results in flow reattachment. In contrast, a decrease in separation angle results in an increase in the separation region. The increase in separation angle coincided with an increase in lift and a reduction in drag. Thus, a pulse location yielding a greater increase in lift corresponded to a greater degree of reattachment, providing guidance on actuator selection for separation control. These qualitative analyses on actuator selection would benefit from a systematic and quantitative approach grounded in optimal control theory. Further, a

purely data-driven approach would ensure that the actuator selection method can be applied within the context of both numerical simulations and physical experiments.

In this paper, we present a data-driven technique for determining the optimal actuator location for driving a quantity of interest (e.g., lift or separation angle) with minimal control effort. The only requirement for the approach is a collection of input-output response data associated with a set of candidate actuator locations, making the approach attractive for both numerical and experimental studies. The Eigensystem Realization Algorithm (ERA) [40] is used to extract a system model that describes the dynamic response data. This description is then used to solve a minimum energy optimal control problem, which yields an objective measure for comparing the relative performance of each actuator location in controlling the quantity of interest. The specific measure we propose is based on the generalized output controllability Gramian, which is valid for both stable and unstable systems. This makes for a versatile approach that can be applied to general systems.

The optimal actuator selection method is applied to high-fidelity numerical data from [39], corresponding to the lift $C_\ell(t)$ and separation angle $\theta(t)$ responses due to a pulse of localized body-force actuation at six distinct locations on the upper-surface of a NACA 65(1)-412 airfoil with angle of attack $\alpha = 4^\circ$ and chord-based Reynolds number $Re_c = 20,000$ (see Figure 1). The optimal actuator locations for controlling lift and separation angle are found to be different. As such, we introduce a DMD-based controllability analysis to identify flow structures that are most sensitive to the actuation. This analysis sheds light on physical mechanisms that explain these differences in the actuator selection results. The results suggest that the separation angle can be controlled more easily than lift, provided that actuation is applied at the optimal location.

The paper is organized as follows: In Section 2, we present the optimality measure and necessary mathematical machinery for conducting a data-driven analysis. In Section 3, the method is applied to analyze the data in Figure 1 to determine the optimal actuator location for controlling lift and separation angle on a NACA 65(1)-412 airfoil. We also introduce and use a DMD-based controllability analysis of the flowfield response to identify physical mechanisms that can explain the actuator selection results. Conclusions are presented in Section 4.

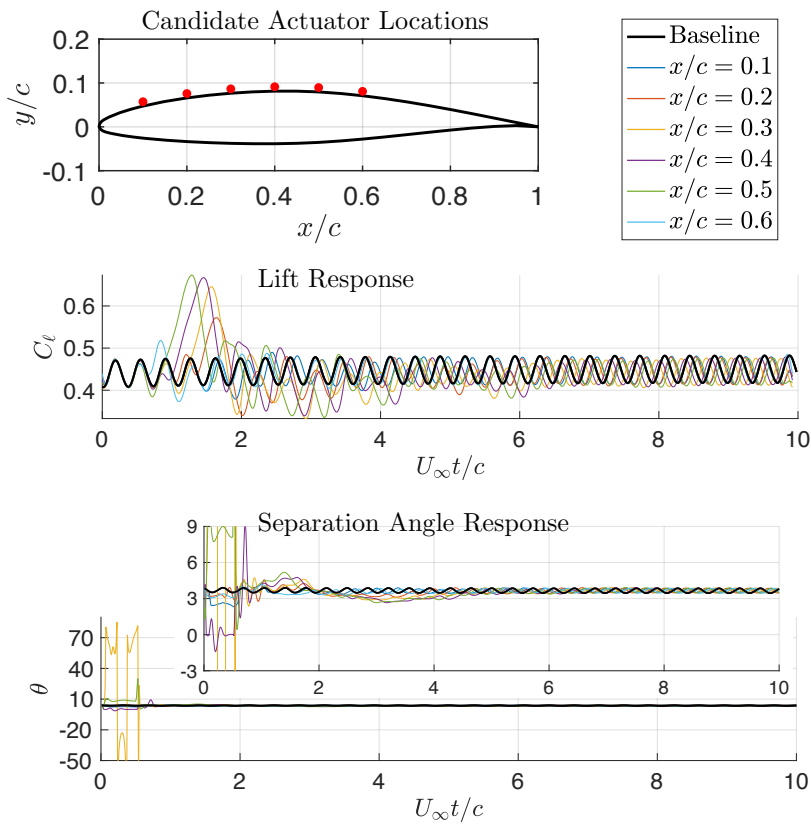


Fig. 1: Lift and separation angle response data due to a pulse of localized body-force actuation at each of six candidate locations on a NACA 65(1)-412 airfoil. High-fidelity numerical simulation data courtesy of [39].

2 Methodology

Consider a finite-dimensional state-space realization $G = (A, B, C)$ representing the dynamic response from a single actuator input $u(t)$ to a single output quantity of interest $y(t)$:

$$\begin{aligned}\dot{x}(t) &= Ax(t) + Bu(t) \\ y(t) &= Cx(t).\end{aligned}\tag{1}$$

Here, $x \in \mathbb{R}^n$ is the n -dimensional state vector. We assume that $G = (A, B, C)$ is minimal (i.e., it is both controllable and observable). It will be shown how such a realization can be determined from data in Section 2.2.

We seek the control input $u^{\text{opt}}(t)$ that drives the system state from the origin to an arbitrary point in state-space with minimal control energy over an infinite time-horizon¹. This optimal control problem can be solved by standard methods and is commonly referred to as the *minimum control energy problem* [41]:

$$\begin{aligned}\text{minimize} \quad & J = \int_0^\infty u^\top(\tau)u(\tau)d\tau \\ \text{subject to} \quad & \dot{x}(t) = Ax(t) + Bu(t) \\ & x(0) = 0 \\ & x(\infty) = x_f,\end{aligned}\tag{2}$$

which admits a solution if the system is controllable. The minimal input energy associated with the optimal control is given by,

$$J^{\text{opt}} = x_f^\top W_c^{-1} x_f,\tag{3}$$

¹ Although finite time-horizons can be considered, we choose to focus on the infinite time-horizon case in order to maintain objectivity in the optimality measure; the solution to the finite time-horizon problem is dependent on the final time, which can be undesirable because the final time can always be chosen to influence the outcome of the optimality measure.

where the controllability Gramian

$$W_c := \int_0^\infty e^{A\tau} B B^\top e^{A^\top \tau} d\tau \quad (4)$$

is the stabilizing solution to the Lyapunov equation,

$$A W_c + W_c A^\top + B B^\top = 0 \quad (5)$$

To determine the actuator location that yields the minimum control energy, we can simply compare the relative sizes of W_c corresponding to the dynamics of each actuator location—a larger W_c being more controllable and requiring less input energy to control. Note that the controllability Gramian W_c is not invariant under similarity transformation. This is an important point to consider when system realizations $G = (A, B, C)$ are obtained from data, as will be discussed in Section 2.2. In such instances, care must be taken when formulating measures of optimality directly based on W_c . Some suitable choices that are invariant under similarity transformation are, e.g., $\det(W_c)$, $\text{trace}(W_c)$.

To gain an intuition for the optimal solution, we can view the quadratic form in (3) as defining an ellipse that contains all points in state-space that can be *reached from the origin* using no greater than unit input energy, $X = \{x_f \in \mathbb{R}^n \mid x_f^\top W_c^{-1} x_f \leq 1\}$. The most controllable directions in state-space require the least control energy to traverse and are related to the eigendirections associated with the largest eigenvalues of W_c ; the least controllable directions in state-space require the most control energy to traverse and are related to the eigendirections associated with the smallest eigenvalues of W_c .

Although, W_c provides intuition about the most controllable directions in state-space, in practice, the quantity of interest may not directly correspond to these states; instead, the quantity of interest corresponds to a specific linear combination of these states: $y(t) = Cx(t)$. Hence, rather than considering the

state controllability Gramian W_c directly, we can instead work with a suitably weighted version of W_c ,

$$W_{oc} := \int_0^\infty C e^{A\tau} B B^\top e^{A^\top \tau} C^\top d\tau \quad (6)$$

$$= C W_c C^\top, \quad (7)$$

which is simply the *output controllability Gramian* [42]. Output controllability is a more natural measure of optimality because it is invariant under similarity transformations, and thus constitutes a system property that is coordinate independent. This choice is particularly appealing because measures based on W_{oc} admit numerous other interpretations, beyond those afforded by the minimum control energy perspective. For instance, the output controllability Gramian is directly related to the \mathcal{H}_2 -norm of a stable LTI system as,

$$\|g(t)\|_2 = \sqrt{\int_0^\infty g(t)^\top g(t) dt} = \sqrt{W_{oc}} \quad (8)$$

where $g(t) := C e^{At} B$ is the impulse response. Further, we can arrive at a frequency-domain interpretation of this measure by invoking Parseval's theorem [43],

$$\|g(t)\|_2 = \|G(s)\|_2 := \sqrt{\frac{1}{2\pi} \int_{-\infty}^\infty (G(-j\omega)^\top G(j\omega)) d\omega} \quad (9)$$

$$= \sqrt{\frac{1}{2\pi} \int_{-\infty}^\infty |G(j\omega)|^2 d\omega} \quad (10)$$

where $G(s)$ denotes the transfer function from the input to the output. Hence, the \mathcal{H}_2 -norm can be interpreted as the average system gain over all forcing frequencies. Consistent with the minimum control energy interpretation, this indicates that a system with a larger \mathcal{H}_2 -norm will tend to yield a larger output for the same input signal. The \mathcal{H}_2 -norm also admits a stochastic interpretation

from the lens of linear quadratic Gaussian (LQG) control [43]: all else equal, a system with a larger \mathcal{H}_2 -norm will yield a larger output power in response to a unit intensity white noise input.

2.1 Generalizability to unstable systems

The \mathcal{H}_2 optimality measure can be generalized to unstable systems. This generalization is useful if we are interested in comparing actuator locations for general systems, which may or may not be stable. Of course, in the context of unstable systems, neither the state controllability Gramian nor the output controllability Gramian will necessarily be bounded; thus, these optimality measures are ill-suited for comparing general flow control configurations that may exhibit unstable dynamics. However, by taking a frequency-domain perspective of the state controllability Gramian, we can arrive at a *generalized controllability Gramian* P that is bounded for unstable systems [44]:

$$P = \frac{1}{2\pi} \int_{-\infty}^{\infty} (j\omega I - A)^{-1} B B^T (-j\omega I - A^T)^{-1} d\omega \quad (11)$$

The generalized controllability Gramian is also related to the minimum control energy problem, as shown in Theorem 5 of [44]. Specifically, when the system under consideration is controllable, $x_o^T P^{-1} x_o = \inf\{\|u\|_2^2 \mid x(0) = x_o, x(-\infty) = 0, x(\infty) = 0\}$. As with W_c , a larger P indicates that less control energy is required to drive the state to the origin from an arbitrary initial state (i.e., the system is “more controllable”). In other words, the generalized controllability Gramian P has an equivalent interpretation as the conventional controllability Gramian W_c , but extends the interpretation to the context of unstable systems. Indeed, when the system under consideration is stable, the generalized controllability Gramian is equivalent to the standard controllability Gramian (i.e., $P = W_c$).

Conveniently, for a stabilizable and detectable system, the generalized controllability Gramian P can be computed directly from a state-space realization of the system. The procedure follows directly from Theorem 2 in Zhou et al. [44], which amounts to solving for the stabilizing solution X to the algebraic Riccati equation,

$$XA + A^T X - XBB^T X = 0 \quad (12)$$

followed by a computation of the generalized controllability Gramian P as the solution to the Lyapunov equation,

$$(A + BF)P + P(A + BF)^T + BB^T = 0, \quad (13)$$

where $F = -B^T X$. For stable systems, $X = 0$ and, therefore, $P = W_c$.

For the purpose of determining a measure of optimality for actuator placement, here we will define the *generalized \mathcal{H}_2 -norm* (denoted $\mathcal{H}_{2'}$) in analogy with Eq. (8), but now using the notion of generalized output controllability CPC^T instead of the conventional output controllability CW_cC^T .

$$\|G\|_{2'} = \sqrt{CPC^T} \quad (14)$$

This measure is related to the output controllability of the system and is often times more desirable, as the end goal is to effectively control the output. Another attractive feature of this measure is that it is invariant to system realizations and is therefore not dependent on the method in which system realizations are obtained.

In the remainder of this paper, $\|G\|_{2'}$ will be used as a measure for determining the optimal actuator location among a set of candidate actuator locations. In our case, this measure is computed for all the candidate locations

using the minimal realization obtained from pulse response data, as will be described in the next subsection.

2.2 Minimal realizations from pulse response data

An imperative step in determining optimality among the candidate set of actuator locations is obtaining mathematical models for the dynamic response from actuator input $u(t)$ to the quantity of interest $y(t)$ for each candidate configuration. Once such system models are obtained, analyses corresponding to optimality can be conducted. The field of system identification deals with obtaining mathematical models for a system based on data observations obtained from the system. In general, such data is usually sampled at discrete instants of time in a large variety of applications. Hence, discrete-time system models show higher suitability for system identification methods. Identified models can be transformed subsequently to continuous-time as needed for further analysis. Here, we describe one such method for determining a minimal discrete-time system realization from empirical pulse response data. These discrete-time state-space realizations are then converted to continuous-time realizations—in the form of (1)—by means of Tustin’s approximation [45].

Consider the discrete-time state-space realization $\hat{G} = (\hat{A}, \hat{B}, \hat{C})$:

$$\begin{aligned} x(k+1) &= \hat{A}x(k) + \hat{B}u(k) \\ y(k) &= \hat{C}x(k) \end{aligned} \tag{15}$$

where $x \in \mathbb{R}^n$ is the state vector, $u \in \mathbb{R}$ is the actuator input, $y \in \mathbb{R}$ is the output quantity of interest, and $k \in \mathbb{Z}$ is the sampling time index. The response of the quantity of interest to a pulse input yields a sequence of scalar

Markov parameters,

$$h_k = \begin{cases} 0 & \text{for } k = 0 \\ \hat{C}\hat{A}^{k-1}\hat{B} & \text{for } k \geq 1. \end{cases} \quad (16)$$

For each candidate actuator location, we appeal to the Eigensystem Realization Algorithm (ERA) [40] to compute a minimal realization of the system $\hat{G} = (\hat{A}, \hat{B}, \hat{C})$ directly from this pulse response data h_k . To do so, we define two Hankel matrices composed of the Markov parameters,

$$H_0 = \begin{bmatrix} h_1 & h_2 & \cdots & h_{n_o} \\ h_2 & h_3 & \cdots & h_{n_o+1} \\ \vdots & \vdots & \ddots & \vdots \\ h_{n_c} & h_{n_c+1} & \cdots & h_{n_c+n_o} \end{bmatrix}, \quad H_1 = \begin{bmatrix} h_2 & h_3 & \cdots & h_{n_o+1} \\ h_3 & h_4 & \cdots & h_{n_o+2} \\ \vdots & \vdots & \ddots & \vdots \\ h_{n_c+1} & h_{n_c+2} & \cdots & h_{n_c+n_o+1} \end{bmatrix}. \quad (17)$$

Next, compute the Singular Value Decomposition (SVD) of $H_0 = U\Sigma V^*$, then store the r largest singular values in a matrix Σ_r and the corresponding left- and right-singular vectors in the matrices U_r and V_r , respectively. Finally, a minimal realization $(\hat{A}, \hat{B}, \hat{C})$ can be computed as,

$$\hat{A} := \Sigma_r^{-\frac{1}{2}} U_r^* H_1 V_r \Sigma_r^{-\frac{1}{2}} \quad (18)$$

$$\hat{B} := \text{First column of } \Sigma_r^{\frac{1}{2}} V_r^* \quad (19)$$

$$\hat{C} := \text{First row of } U_r \Sigma_r^{\frac{1}{2}} \quad (20)$$

A complete description of ERA can be found in [40]. As was shown in the previous subsection, the \mathcal{H}_2 -norm optimality measure associated with each actuator location can then be computed directly from this ERA-based minimal realization.

Our choice of utilizing pulse response data for system identification is quite natural since Markov parameters have the property of being unique for a given system and are often referred to as the “signature” of the system model [46]. In the event that other forms of input-output data are available through simulations/experiments, methods such as Observer/Kalman Filter Identification (OKID) may be used to extend the applicability of ERA to general input-output response data [47]. We note that ERA introduces some elements of subjectivity to the optimal selection process, since various ERA algorithm parameters, such as n_c , n_o can be chosen to alter the specific realization; however, additional precautions can be taken to ensure that the realization is sufficiently insensitive to these algorithmic parameters and that multiple ERA realizations based on the same pulse response data yield consistent optimal actuator rankings. Indeed, this will be the case for all of the results that are reported in Section 3.

We further note that ERA is applicable for both stable and unstable systems [48]. In principle, it is possible to compute the output controllability Gramian by direct integration of pulse response data; however, performing a direct integration of pulse response data for unstable systems (or of un-converged responses in general) over an infinite time-horizon is not possible. Appealing to generalized Gramians computed via ERA system realizations overcomes this challenge.

3 Results

We apply the approach described in Section 2 to the numerical pulse response data shown in Figure 1 to determine the optimal actuator location for controlling lift and separation angle. For clarity, we first outline the specific steps

involved in determining the optimal actuator location when the quantity of interest is the lift C_ℓ :

1. *Collect Data.* Collect sampled pulse response data $C_\ell^i(k)$ for each of the $i = 1, \dots, N$ candidate actuator locations. Also, collect the uncontrolled baseline lift response $C_\ell^0(k)$ and compute its mean $\overline{C_\ell^0}$.
2. *Form Markov Parameters.* Subtract the uncontrolled baseline mean from each pulse response signal to obtain the associated sequence of Markov parameters $h_k^i = C_\ell^i(k) - \overline{C_\ell^0}$.
3. *Identify System Realizations.* Perform ERA on each sequence h_k^i to obtain a discrete-time system realization $\hat{G}^i = (\hat{A}^i, \hat{B}^i, \hat{C}^i)$. Convert this realization to a continuous-time realization $G^i = (A^i, B^i, C^i)$ via Tustin's approximation.
4. *Compute $\mathcal{H}_{2'}$ Optimality Measures.* For each system realization G^i , compute the generalized controllability Gramian P^i from Equations (12) and (13). From this, compute the optimality measure $\|G^i\|_{2'} = \sqrt{C^i P C^{i\top}}$ for each actuator location.
5. *Select Optimal Actuator.* Sort actuators according to decreasing $\mathcal{H}_{2'}$ -norm. The optimal actuator location is the one associated with the largest value of $\|G^i\|_{2'}$.

The same procedure can be applied to analyze the optimal actuator location for controlling separation angle. To do so, simply substitute $C_\ell \leftarrow \theta$ everywhere above.

We first perform steps 1–3 above for the lift and separation angle responses. An ERA model of order r is realized for each actuator location and each quantity of interest (see Figures 3 and 6). Here, r is chosen to give the best match in terms of the original data obtained from numerical simulations. As previously indicated, a number of these realizations exhibit unstable dynamics, with some

of the discrete-time poles lying outside the unit circle in Figures 2 and 5. This motivates the use of generalized controllability Gramians and the associated \mathcal{H}_2 for the subsequent analysis. We note that the unstable realizations may be related to the slow asymptotic return to the baseline response. This point is supported by the fact that realizations computed using shorter time-horizons result in unstable modes that are “more unstable”. The minimality and order of ERA-based realizations were sanitized of any potential numerical artificialities by accounting for pole-zero cancellations based on a range of tolerances from $\mathcal{O}(10^{-5})$ to $\mathcal{O}(10^{-7})$. These tolerance values indicate the proximity of poles and zeros required to constitute a numerical pole-zero cancellation. Tolerances have been selected in conjunction with the system order r to ensure the realization is minimal and able to describe the given response data.

We next perform steps 4–5 in the selection process outlined above. The \mathcal{H}_2 -norms associated with each actuator location are sorted from most controllable to least controllable and reported in Tables 1 and 2. The optimal actuator location for lift control is found to be $x/c = 0.2$, whereas for separation angle control it is found to be $x/c = 0.3$. The ranking of actuators and further analysis of these results is presented for lift in Section 3.1 and for separation angle in Section 3.2. A modal analysis of the flowfield is conducted in Section 3.3 to help identify physical mechanisms underlying these observations.

3.1 Optimal actuator placement for controlling lift

Based on the \mathcal{H}_2 -norm, the optimal actuator location for lift control is $x/c = 0.2$. This location has the highest controllability among all six candidate locations. The optimality study considered tolerance values for pole-zero overlap of $\mathcal{O}(10^{-5})$ to $\mathcal{O}(10^{-7})$. The optimal actuator position is largely con-

stant with these tolerances, although minor variations in the relative ranking of other actuators are observed in the case of lift control. Some of the eigenvalues of the discrete-time realizations obtained are outside the unit circle for all actuator locations, thereby confirming that the identified systems are unstable (see Figure 2). As can be seen in Figure 3, the high order for the obtained minimal realizations, in all likelihood indicates that the system may have some degree of non-linearity in it, which is captured by a larger number of states. The peak frequency for all actuator locations is $fc/U_\infty = 6.12$, as can be seen in Figure 4 and corresponds to the wake frequency. Thus, it appears that among all actuator locations, $x/c = 0.2$ is able to induce a resonance by coupling with the flow dynamics at this forcing frequency.

x/c	$\ G\ _{2'}$
.2	51.79
.6	31.31
.1	17.41
.5	15.81
.4	15.41
.3	13.41

Table 1: Optimality of actuator locations based on the generalized \mathcal{H}_2 -norm, sorted from most to least optimal for different tolerance values used in minimal realization for lift response data.

3.2 Optimal actuator placement for controlling separation angle

A similar exercise as described above is also undertaken for the separation angle pulse response data. Based on the \mathcal{H}_2 -norm, the optimal actuator location for separation angle control is $x/c = 0.3$ (see Table 2). This location has a degree of controllability which is significantly larger than other locations. The related norm for this actuator location is an order of magnitude greater than the next optimal location. This is also reflected in the very high response peak

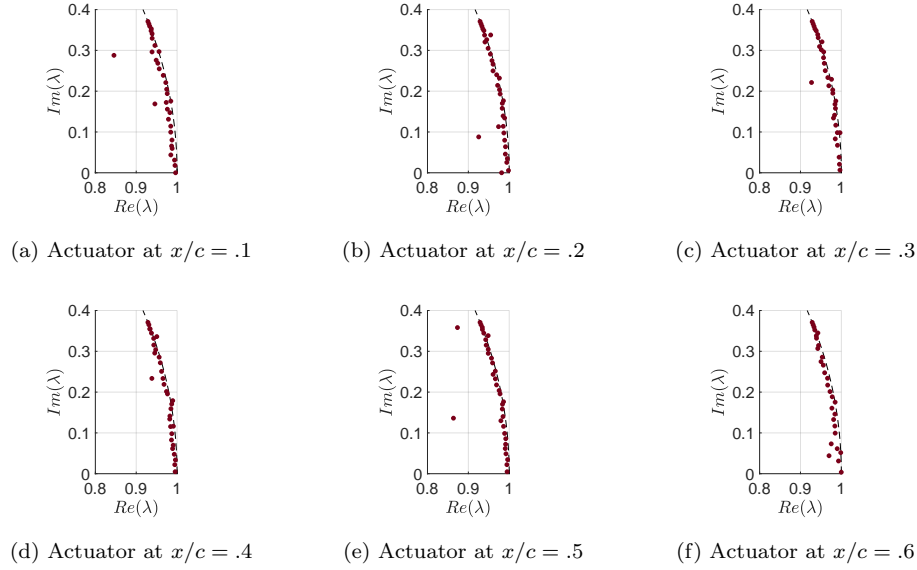


Fig. 2: System poles of (discrete-time) minimal realization computed from pulse response data for each actuator location using ERA for lift response data. Some poles are outside the unit circle for all locations.

associated with this location as compared to the other candidate locations (see Figure 6). Note that the next optimal location is $x/c = 0.5$, which coincides with the asymptotic separation point itself [39].

The results provide two interesting observations. First, the order of the minimal realizations obtained for the separation angle responses are an order of magnitude above the realizations associated with the lift responses. This suggests a greater degree of non-linearity associated with separation angle response than with lift response. Consistently, generalized \mathcal{H}_2 -norms associated with these candidate locations (see Table 2) are greater than their lift counterparts. This is especially prominent for the higher ranked locations in the separation angle case.

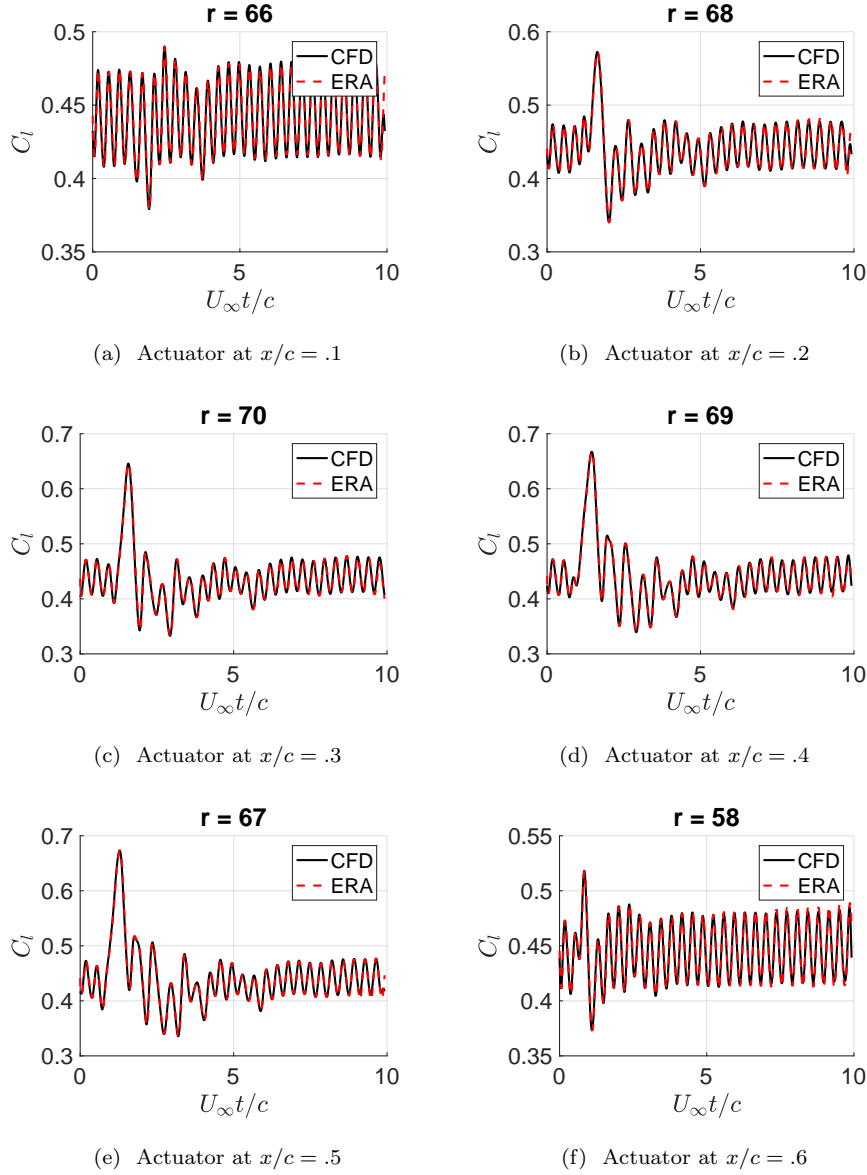


Fig. 3: Lift coefficient pulse response data at each actuator location. Each realization is minimal with order r .

x/c	$\ G\ _{2'}$
.3	1.63×10^7
.5	3.99×10^4
.4	1059.57
.1	243.24
.6	91.95
.2	76.74

Table 2: Optimality of actuator locations based on the generalized \mathcal{H}_2 -norm, sorted from most to least optimal for different tolerance values used in minimal realization for separation angle response data.

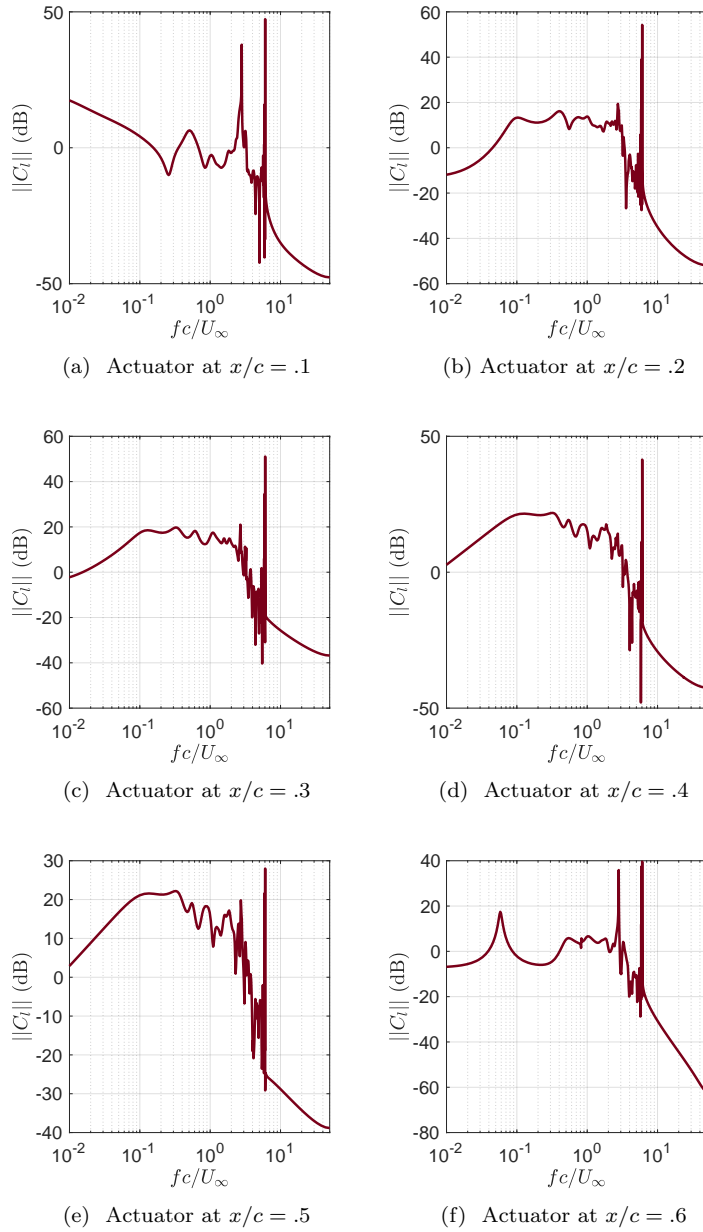


Fig. 4: Bode magnitude plot for minimal realization at each actuator location for lift response data.

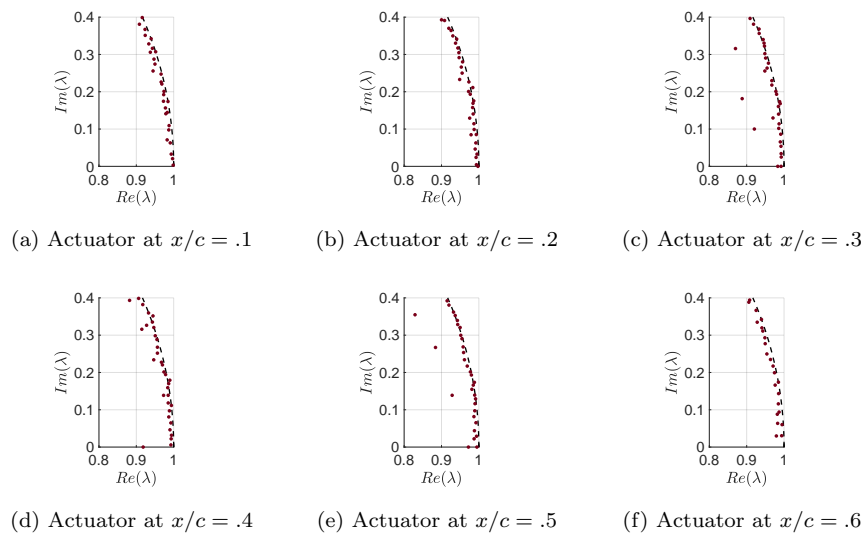


Fig. 5: System poles of (discrete-time) minimal realization computed from separation angle pulse response data for each actuator location using ERA. Some poles are outside the unit circle for all locations.

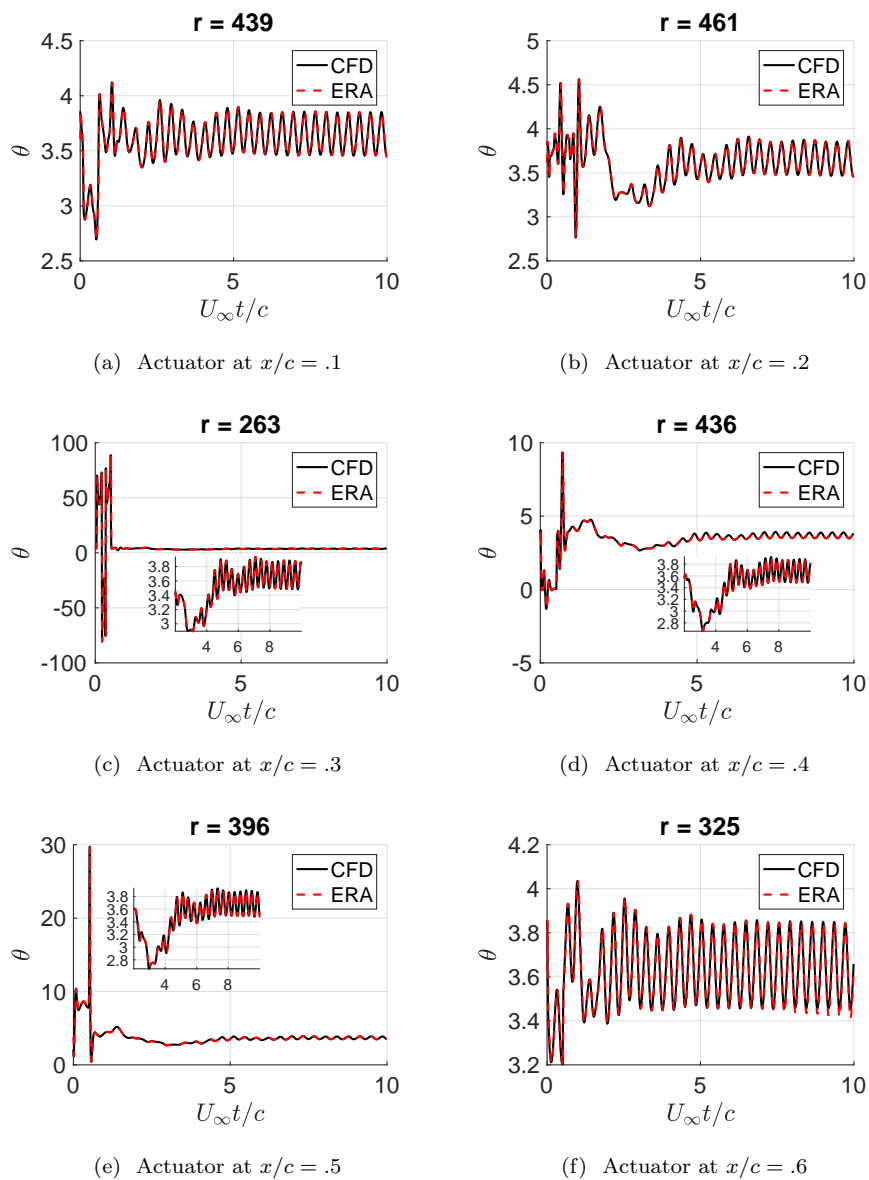


Fig. 6: Separation angle pulse response data at each actuator location. Each realization is minimal with order r .

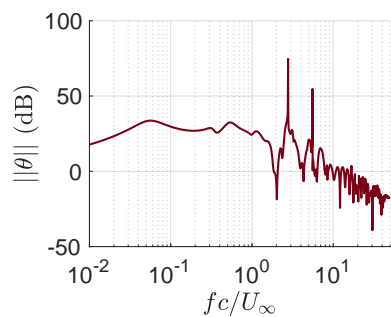
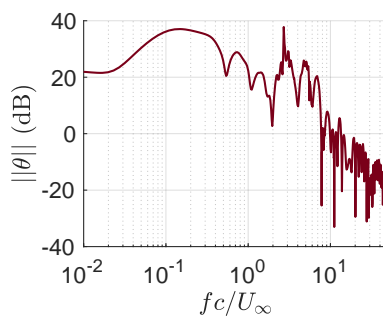
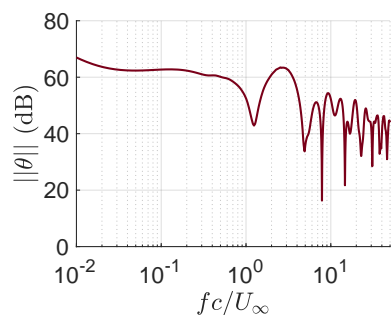
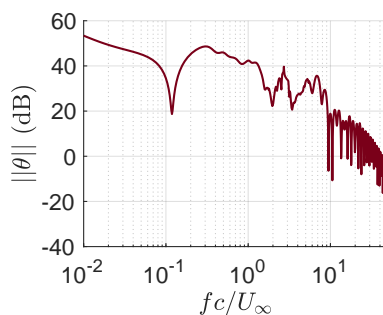
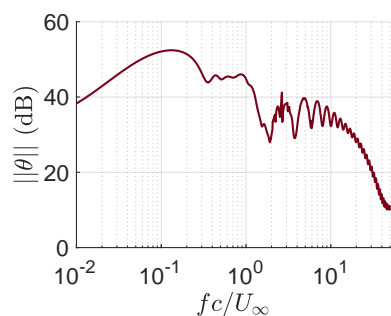
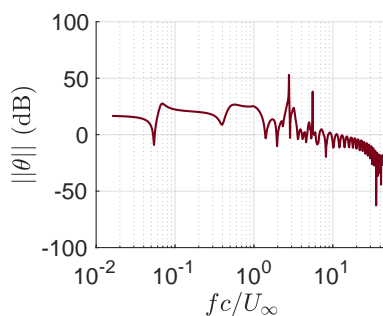
(a) Actuator at $x/c = .1$ (b) Actuator at $x/c = .2$ (c) Actuator at $x/c = .3$ (d) Actuator at $x/c = .4$ (e) Actuator at $x/c = .5$ (f) Actuator at $x/c = .6$

Fig. 7: Bode magnitude plot for minimal realization at each actuator location for the separation angle response.

3.3 Modal Analysis of the Flowfield Response

To understand *why* the actuator locations for controlling separation angle and lift are optimal, we perform modal analysis of the flowfield and attempt to understand the underlying physical mechanisms.

We leverage the dynamic mode decomposition (DMD) to extract dynamically meaningful spatio-temporal information from snapshot data of the dynamic response of the flowfield [49–51]. In particular, we use the DMD with control (DMDc) algorithm [52] in order to properly account for the influence of external forcing on the flow from actuation. DMDc is a data-driven method that is closely related to ERA [52]; however, DMDc assumes access to the full-state output, whereas ERA does not. Further, DMDc requires additional care when data are gathered from physical experiments, as measurement noise can introduce bias errors that must be taken into account [28, 53–55].

At its heart, DMDc approximates flow response data with a dynamical system of the form,

$$x(k+1) = \hat{A}x(k) + \hat{B}u(k). \quad (21)$$

Here, we take $x(k) \in \mathbb{R}^n$ to be a snapshot of the velocity field at time-step k and $u(k) \in \mathbb{R}$ as the associated input. For a unit pulse of body-force actuation applied at a single location on the airfoil at $k = 0$, this corresponds to $u(0) = 1$ and $u(k) = 0$ for $k \geq 1$. Response data are collected and stored in data matrices of state and input sequences,

$$X = \begin{bmatrix} x(1) & x(2) & \cdots & x(m) \end{bmatrix} \quad (22)$$

$$X' = \begin{bmatrix} x(2) & x(3) & \cdots & x(m+1) \end{bmatrix} \quad (23)$$

$$Y = \begin{bmatrix} u(1) & u(2) & \cdots & u(m) \end{bmatrix}. \quad (24)$$

Then, DMDC approximates the underlying system dynamics (\hat{A}, \hat{B}) as a least-squares/minimum-norm solution to $X' \approx \hat{A}X + \hat{B}\Upsilon$ [52]. Specifically,

$$\begin{bmatrix} \hat{A} \\ \hat{B} \end{bmatrix} \approx X' \underbrace{\begin{bmatrix} X \\ \Upsilon \end{bmatrix}}_{\Omega} = \begin{bmatrix} \underbrace{X' \tilde{V} \tilde{\Sigma}^{-1} \tilde{U}_1^T}_{\bar{A}} & \underbrace{X' \tilde{V} \tilde{\Sigma}^{-1} \tilde{U}_2^T}_{\bar{B}} \end{bmatrix}, \quad (25)$$

where the truncated SVD gives a rank- p approximation of $\Omega \approx \tilde{U} \tilde{\Sigma} \tilde{V}^T$, $\tilde{U}^T = \begin{bmatrix} \tilde{U}_1^T & \tilde{U}_2^T \end{bmatrix}$, $\tilde{U}_1 \in \mathbb{R}^{n \times p}$, $\tilde{U}_2 \in \mathbb{R}^{1 \times p}$, $\bar{A} \approx \hat{A}$, and $\bar{B} \approx \hat{B}$. Since n is large in fluids applications, DMDC works with a reduced-order representation of the dynamics,

$$\tilde{x}(k+1) = \tilde{A}\tilde{x}(k) + \tilde{B}u(k), \quad (26)$$

where $x = \hat{U}\tilde{x}$, $\tilde{A} = \hat{U}^T \bar{A} \hat{U}$, $\tilde{B} = \hat{U}^T \bar{B}$, and $\hat{U} \in \mathbb{R}^{n \times r}$ is determined from a rank- r approximation of X' computed via the truncated SVD of $X' \approx \hat{U} \hat{\Sigma} \hat{V}^T$. It follows that the eigenvectors v and eigenvalues λ of \tilde{A} are related to the eigenvectors ϕ (DMD modes) and eigenvalues λ (DMD eigenvalues) of \bar{A} [52]. It is also possible to relate the left-eigenvectors w of \tilde{A} to the left eigenvectors ψ (adjoint DMD modes) of \bar{A} , as noted in [51] and [56]. The DMDC algorithm is summarized as,

1. Collect data and form the relevant data matrices X , X' , and Υ defined in Equations (23)–(24), respectively.
2. Compute the rank- p truncated SVD

$$\Omega = \begin{bmatrix} X \\ \Upsilon \end{bmatrix} \approx \tilde{U} \tilde{\Sigma} \tilde{V}^*. \quad (27)$$

3. Compute the rank- r truncated SVD $X' \approx \hat{U} \hat{\Sigma} \hat{V}^*$, where $r < p$.

4. Compute the reduced-order system realization

$$\tilde{A} = \hat{U}^* X' \tilde{V} \tilde{\Sigma}^{-1} \tilde{U}_1^* \hat{U} \quad (28)$$

$$\tilde{B} = \hat{U}^* X' \tilde{V} \tilde{\Sigma}^{-1} \tilde{U}_2 \quad (29)$$

5. Compute the eigendecompositions $\tilde{A}v_i = \lambda_i v_i$ and $\tilde{A}^T w_i = \lambda_i w_i$. The DMD eigenvalues λ_i can be used to determine the associated modal frequencies $\angle \lambda_i / (2\pi \delta t)$ and growth/decay rates $\log |\lambda_i| / \delta t$, where δt is the sampling time. The DMD mode corresponding to each DMD eigenvalue λ_i is computed as $\phi_i = X' \tilde{V} \tilde{\Sigma}^{-1} \tilde{U}_1^* \hat{U} v_i$.

Further details about DMDc can be found in [52].

Performing DMDc on velocity field response data due to pulse actuation applied at $x/c = 0.2$ and 0.3 yields realizations (\tilde{A}, \tilde{B}) of order $r = 300$. Recall, these locations are found to be optimal for lift and separation angle control, respectively. DMD eigenvalues for actuator locations $x/c = 0.2$ and $x/c = 0.3$ are shown in Figure 8.

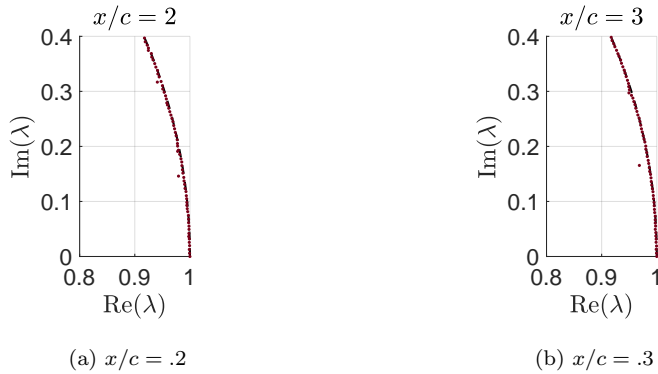


Fig. 8: DMD Eigenvalues for actuator locations $x/c = 0.2$ and $x/c = 0.3$

We note that $w_i^T \tilde{B}$ provides information about the controllability of the DMD mode ϕ_i . This, in fact, is closely related to the well-established modal controllability test of Popov, Belevitch, and Hautus (PBH) [57]. Here, we invoke a measure of modal controllability for linear systems proposed in [58],

$$\gamma_i = \frac{|w_i^T \tilde{B}|}{\|w_i\| \|\tilde{B}\|} \quad (30)$$

where \tilde{B} is a column vector in this study because there is only one input channel per realization. Then, the measure γ_i corresponds to the cosine of the (acute) angle between the two one-dimensional subspaces defined by w_i and B . If the two subspaces are orthogonal, then $\gamma_i = 0$, indicating that the DMD mode ϕ_i is uncontrollable from the input. On the other hand, if the two subspaces are perfectly aligned, then $\gamma_i = 1$, indicating that DMD mode ϕ_i is maximally controllable. We note that for multi-input systems, one must consider modal controllability from each available input channel. In such instances, a measure of gross modal controllability can be defined to account for the relative norms of columns in \tilde{B} . Further details can be found in [58].

Using this procedure, we sort DMD modes according to their relative controllability measures. The magnitude of the most controllable DMD modes for actuator locations $x/c = 0.2$ and $x/c = 0.3$ are plotted in Figure 9. For $x/c = 0.2$ —the optimal location for lift control—the most controllable DMD mode is strongly active within the separation bubble and into the wake near the trailing edge of the airfoil. This suggests that the separation bubble and near-wake are most receptive to actuation that benefits lift control. In contrast, the most controllable DMD mode for $x/c = 0.3$ —optimal for separation angle control—is most active in the shear layer and in the wake. Indeed, this mode shows evidence of vortical structures within the shear layer that are effectively manipulated via control at $x/c = 0.3$. This observation suggests that vortex

roll-up within the shear layer provides a mechanism that benefits separation angle control.

Since DMD modes are single-frequency flow structures, the frequencies associated with the most controllable DMD modes may serve as good candidate frequencies for open-loop control using sinusoidal forcing. Further, we note that the frequencies associated with the most controllable DMD modes are consistent with the peaks in the separation angle frequency response determined via ERA (see Figure 7). This finding supports our earlier claim that controlling the separation angle may prove to be more effective than controlling lift directly.

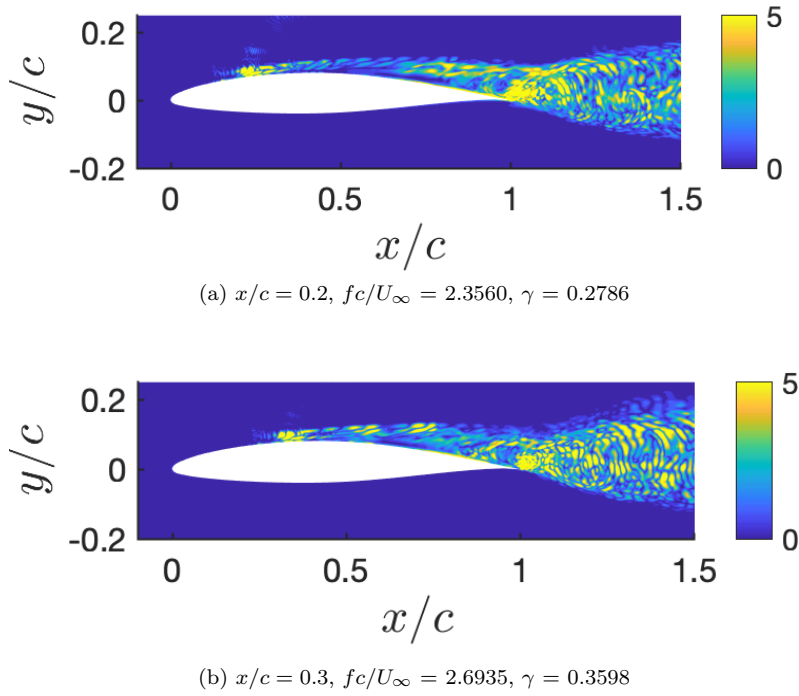


Fig. 9: The magnitude of the most controllable DMD mode associated with actuation at $x/c = 0.2$ and $x/c = 0.3$, visualized using vorticity.

Next, we leverage the generalized controllability Gramian P to determine the most controllable directions in state-space. To do so, we first transform the discrete-time DMDC system realization (\tilde{A}, \tilde{B}) to the associated continuous-time realization, then compute the generalized controllability Gramian directly from Eq. (12) and (13). The principal directions of P can be used to reveal the flow structures that are most sensitive to control action. In particular, the most controllable flow structures are associated with the one-dimensional subspace spanned by

$$\xi_P = X' \tilde{V} \tilde{\Sigma}^{-1} \tilde{U}_1^T \hat{U} v_P, \quad (31)$$

where v_P is the eigendirection associated with the largest eigenvalue of P .

The most controllable flow structures for actuator location $x/c = 0.2$ and $x/c = 0.3$ are shown in Figure 10. Unlike the most controllable DMD modes, the most controllable flow structures identified by this Gramian-based analysis are not associated with just a single-frequency; rather, these structures can exhibit rich dynamics that are associated with evolution along the most controllable direction in state-space. As such, the controllable subspace reveals a different description of control mechanisms than the modal controllability analysis. The optimal actuator location for lift control appears to activate vortex shedding in the wake, starting immediately at the trailing edge of the airfoil. This is consistent with the modal controllability analysis for actuation at $x/c = 0.2$. The fact that the wake is most sensitive to actuation at $x/c = 0.2$ is also consistent with physical intuition, since the transfer of bound vorticity into free vorticity in the wake is the physical mechanism for lift production. For separation angle control, the Gramian-based analysis reveals complex dynamics between the rear of the shear layer, the separation bubble, and the near-wake. The fact gives a slightly different picture than what was observed in the modal controllability analysis. These differences suggest that the dynam-

ics governing the separation angle response are highly nonlinear compared to the dynamics governing the lift response. Further, both the modal controllability analysis and this Gramian-based analysis suggests that actuation at $x/c = 0.3$ can make regions in the shear layer more controllable. As pointed out by several other studies, the shear layer plays a key role in the optimal control of fluid-flows. Several studies have suggested actuating the flow at the shear layer frequency for better control of coherent structures. The results presented here provide evidence to believe that the actuator placed at $x/c = 0.3$ is able to excite the fluid flow more effectively in these regions and hence provide greater controllability.

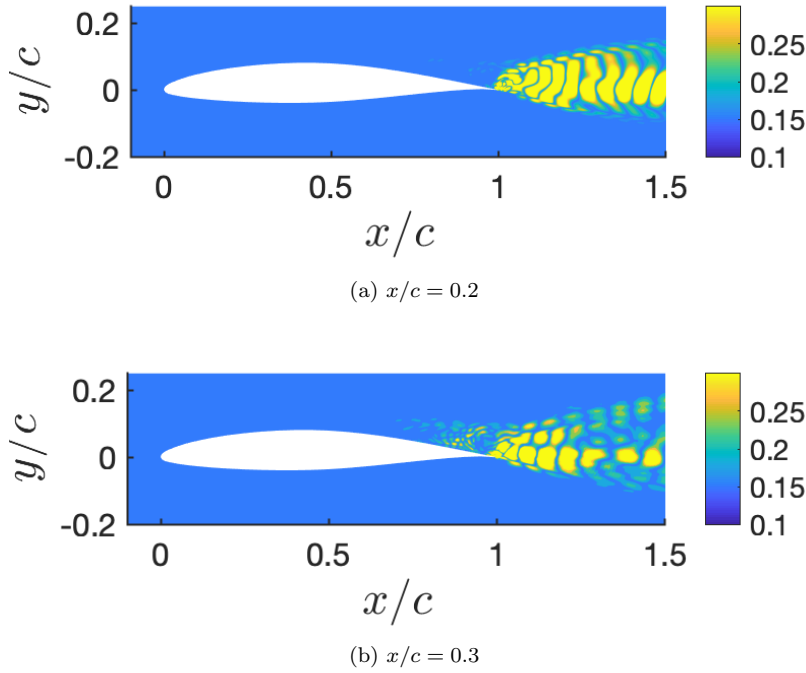


Fig. 10: The magnitude of the first principal direction of the generalized controllability Gramian associated with actuation at $x/c = 0.2$ and $x/c = 0.3$, visualized using vorticity.

4 Conclusion

We presented a data-driven approach for determining the actuator location requiring the minimum control energy to drive an output quantity-of-interest. Given input-output response data for a candidate set of actuator locations, the eigensystem realization algorithm was used to extract state-space system descriptions suitable for solving a minimum input energy optimal control problem and computing the generalized \mathcal{H}_2 -norm for each location. The method only requires access to input-output response data, making it relevant for numerical and experimental studies alike. The method was used to investigate the optimal actuator location for airfoil separation control using data from high-fidelity numerical simulations of a NACA 65(1)-412 airfoil, with $\alpha = 4^\circ$ and $Re_c = 20,000$. Lift and separation angle response data to a pulse of localized body force actuation were used to determine the optimal location among a candidate set of six locations on the upper surface of the airfoil. It was found that the location $x/c = 0.2$ was optimal for controlling lift, whereas the location $x/c = 0.3$ was found to be optimal for controlling separation angle. The analysis also revealed separation angle to be more sensitive than lift to actuation from the associated optimal location, making separation angle the more attractive quantity to regulate in separation control applications.

In order to identify physical mechanisms underlying these results, we presented a data-driven framework for conducting controllability analysis of the flowfield using dynamic mode decomposition with control (DMDc). A controllability analysis of the dominant single-frequency DMD modes confirmed greater controllability for the actuator placed at $x/c = 0.3$, which was the optimal location for separation angle control. Actuation from this location was found to excited flow structures within the shear layer, corroborating previous findings on the effectiveness of shear layer excitation for separation control. A

complementary analysis of the controllable subspaces in the flowfield dynamics confirmed that coherent structures in shear layer were most sensitive to actuation applied at the optimal location for separation control ($x/c = 0.3$). In contrast, coherent structures in the wake were most sensitive to actuation applied at the optimal location for lift control ($x/c = 0.2$).

The methods introduced in this paper are generally applicable for optimal actuator selection and controllability analysis.

A distinctive feature of the proposed optimal actuator selection method is that it is entirely data-driven. The approach does not require access to primal or adjoint simulations, which are often required to conduct similar analyses. This makes for a convenient analysis procedure that can be used to objectively assess the optimal actuator location from available or easy-to-acquire response data. Further, the data-driven nature of the method also makes it generally applicable, and should benefit investigations of other flow control configurations as well.

Acknowledgements

This material is based upon work supported by the Air Force Office of Scientific Research under awards FA9550-16-1-0392, FA9550-17-1-0252, and FA9550-19-1-0034 monitored by Drs. Douglas R. Smith and Gregg Abate. The authors thank Dr. Kevin K. Chen for initial discussions related to optimal actuator selection.

References

1. Gad-el-Hak, M., *Flow Control: Passive, Active, and Reactive Flow Management*, Cambridge University Press, Cambridge, United Kingdom, 2000.

2. Williams, D. R. and MacMynowski, D. G., “Brief history of flow control,” *Fundamentals and Applications of Modern Flow Control*, edited by R. D. Joslin and D. N. Miller, chap. 1, American Institute of Aeronautics and Astronautics, Reston, VA, 2009, pp. 1–20.
3. Cattafesta, L. N. and Sheplak, M., “Actuators for active flow control,” *Annual Review of Fluid Mechanics*, Vol. 43, 2011, pp. 247–272.
4. Sosa, R., Artana, G., Moreau, E., and Touchard, G., “Stall control at high angle of attack with plasma sheet actuators,” *Experiments in fluids*, Vol. 42, No. 1, 2007, pp. 143–167.
5. Little, J. and Samimy, M., “High-lift airfoil separation with dielectric barrier discharge plasma actuation,” *AIAA journal*, Vol. 48, No. 12, 2010, pp. 2884–2898.
6. Mabe, J., Calkins, F., Wesley, B., Woszidlo, R., Taubert, L., and Wygnanski, I., “Single dielectric barrier discharge plasma actuators for improved airfoil performance,” *Journal of Aircraft*, Vol. 46, No. 3, 2009.
7. Cerretelli, C. and Kirtley, K., “Boundary Layer Separation Control with Fluidic Oscillators,” *Journal of Turbomachinery*, Vol. 131, No. 4, 2009.
8. Gregory, J. and Tomac, M. N., “A Review of Fluidic Oscillator Development,” *AIAA Paper 2013-2474*, 2013.
9. Woszidlo, R. and Wygnanski, I., “Parameters Governing Separation Control with Sweeping Jet Actuators,” *AIAA Paper 2011-3172*, 2011.
10. Seo, J. H., Zhu, C., and Mittal, R., “Flow Physics and Frequency Scaling of Sweeping Jet Fluidic Oscillators,” *AIAA Journal*, Vol. 56, No. 6, 2018, pp. 2208–2219.
11. Ostermann, F., Woszidlo, R., Nayeri, C. N., and Paschereit, C. O., “The Interaction Between a Spatially Oscillating Jet Emitted by a Fluidic Oscillator and a Crossflow,” *Journal of Fluid Mechanics*, 2018.

12. Amitay, M., Smith, B., and Glezer, A., "Aerodynamic flow control using synthetic jet technology," *36th AIAA Aerospace Sciences Meeting and Exhibit*, 1998.
13. Glezer, A. and Amitay, M., "Synthetic jets," *Annual review of fluid mechanics*, Vol. 34, No. 1, 2002, pp. 503–529.
14. Hemati, M., Deem, E., Williams, M., Rowley, C. W., and Cattafesta, L. N., "Improving separation control with noise-robust variants of dynamic mode decomposition," *54th AIAA Aerospace Sciences Meeting*, 2016, p. 1103.
15. Deem, E., Cattafesta, L., Yao, H., Hemati, M., Zhang, H., and Rowley, C., "Experimental Implementation of Modal Approaches for Autonomous Reattachment of Separated Flows," *AIAA Aerospace Sciences Meeting*, 2018, pp. AIAA Paper 2018–1052.
16. Seo, J., Cadieux, F., Mittal, R., Deem, E., and Cattafesta, L., "Effect of synthetic jet modulation schemes on the reduction of a laminar separation bubble," *Physical Review Fluids*, Vol. 3, No. 033901, 2018.
17. Seifert, A., Bachar, T., Koss, D., Shepshelovich, M., and Wygnanski, I., "Oscillatory blowing: A tool to delay boundary-layer separation," *AIAA Journal*, Vol. 31, No. 11, 1993.
18. Yarusevych, S., Kawall, J., and Sullivan, P. E., "Airfoil performance at low Reynolds numbers in the presence of periodic disturbances," *Journal of fluids engineering*, Vol. 128, No. 3, 2006.
19. Postl, D., Balzer, W., and Fasel, H., "Control of laminar separation using pulsed vortex generator jets: Direct numerical simulations," *Journal of Fluid Mechanics*, Vol. 676, 2011.
20. Marxen, O., Kotapati, R., Mittal, R., and Zaki, T., "Stability analysis of separated flows subject to control by zero-net-mass-flux jet," *Physics of Fluids*, Vol. 27, No. 2, 2015.

21. Yarusevych, S. and Kotsonis, M., “Steady and transient response of a laminar separation bubble to controlled disturbances,” *Journal of Fluid Mechanics*, Vol. 813, 2017.
22. Raju, R., Mittal, R., and Cattafesta, L., “Dynamics of airfoil separation control using zero-net mass-flux forcing,” *AIAA Journal*, Vol. 46, No. 12, 2008.
23. Mittal, R. and Kotapati, R. B., “Resonant mode interaction in a canonical separated flow,” *IUTAM Symposium on Laminar-Turbulent Transition*, Springer, 2006, pp. 341–348.
24. Mittal, R., Kotapati, R., and Cattafesta, L., “Numerical study of resonant interactions and flow control in a canonical separated flow,” *43rd AIAA Aerospace Sciences Meeting and Exhibit, AIAA 2005-1261*, 2005.
25. Yeh, C.-A. and Taira, K., “Resolvent-analysis-based design of airfoil separation control,” *Journal of Fluid Mechanics*, Vol. 867, 2019, pp. 572–610.
26. Taira, K., Hemati, M. S., Brunton, S. L., Sun, Y., Duraisamy, K., Bagheri, S., Dawson, S. T. M., and Yeh, C.-A., “Modal Analysis of Fluid Flows: Applications and Outlook,” 2019, arXiv:1903.05750.
27. Deem, E. A., Cattafesta, L. N., Zhang, H., Rowley, C. W., Hemati, M., Cadieux, F., and Mittal, R., “Identifying dynamic modes of separated flow subject to ZNMF-based control from surface pressure measurements,” *47th AIAA Fluid Dynamics Conference*, 2017, pp. AIAA Paper 2017-3309.
28. Hemati, M. S., Rowley, C. W., Deem, E. A., and Cattafesta, L. N., “De-biasing the dynamic mode decomposition for applied Koopman spectral analysis of noisy datasets,” *Theoretical and Computational Fluid Dynamics*, Vol. 31, No. 4, 2017, pp. 349–368.
29. Chen, K. K. and Rowley, C. W., “H 2 optimal actuator and sensor placement in the linearised complex Ginzburg–Landau system,” *Journal of Fluid Mechanics*, Vol. 681, 2011, pp. 241–260.

30. Chanekar, P. V., Chopra, N., and Azarm, S., “Optimal actuator placement for linear systems with limited number of actuators,” *American Control Conference (ACC), 2017*, IEEE, 2017, pp. 334–339.
31. Manohar, K., Brunton, B., Kutz, J., and Brunton, S., “Data-driven sparse sensor placement for reconstruction: Demonstrating the benefits of exploiting known patterns,” *IEEE Control Systems Magazine*, Vol. 38, No. 3, 2018.
32. Clark, E., Askham, T., Brunton, S. L., and Kutz, J. N., “Greedy Sensor Placement with Cost Constraints,” 2018, arXiv:1805.03717.
33. Yao, H. and Hemati, M., “Advances in Output Feedback Control of Transient Energy Growth in a Linearized Channel Flow,” *AIAA Paper 2019-0882*, 2019.
34. Jeong, P., *Synthetic Jet Flow Control of Two- Dimensional NACA 65(1)-412 Airfoil Flow with Finite- Time Lyapunov Exponent Analysis of Lagrangian Coherent Structures*, Master’s thesis, San Diego State University, San Diego, CA, 2016.
35. Torres, R., *Experimental Study of the use of Synthetic Jet Actuators for Flight Control*, Master’s thesis, San Diego State University, San Diego, CA, 2014.
36. Simpson, R. L., “Junction Flows,” *Annual Review of Fluid Mechanics*, Vol. 33, 2001, pp. 415–433.
37. Haller, G., “Exact theory of unsteady separation for two-dimensional flows,” *Journal of Fluid Mechanics*, Vol. 512, 2004, pp. 257–311.
38. Klose, B. F., Serra, M., and Jacobs, G. B., “The Kinematics of Lagrangian Flow Separation in External Aerodynamics,” 2019, arXiv:1909.04129.
39. Kamphuis, M., Jacobs, G. B., Chen, K., Spedding, G., and Hoeijmakers, H., “Pulse Actuation and Its Effects on Separated Lagrangian Coherent Structures for Flow over a Cambered Airfoil,” *2018 AIAA Aerospace Sci-*

- ences Meeting, AIAA 2018-2255*, 2018.
40. Juang, J.-N. and Pappa, R. S., “An eigensystem realization algorithm for modal parameter identification and model reduction,” *Journal of Guidance*, Vol. 8, No. 5, 1985, pp. 620–627.
 41. Toscano, R., *Structured Controllers for Uncertain Systems: A Stochastic Optimization Approach*, Springer, London, 2013.
 42. Kreindler, E. and Sarachik, P., “On the concepts of controllability and observability of linear systems,” *IEEE Transactions on Automatic Control*, Vol. 9, No. 2, apr 1964, pp. 129–136.
 43. Skogestad, S. and Postlethwaite, I., *Multivariable feedback control: analysis and design*, Vol. 2, Wiley, New York, 2007.
 44. Zhou, K., Salomon, G., and Wu, E., “Balanced Realization and Model Reduction for Unstable Systems,” *International Journal of Robust and Nonlinear Control*, Vol. 9, 1999, pp. 183–198.
 45. Åström, K. J. and Wittenmark, B., *Computer-controlled systems: theory and design*, Prentice-Hall, 1997.
 46. Vicario, F., *OKID as a general approach to linear and bilinear system identification*, Columbia University, 2014.
 47. Juang, J.-N., Phan, M. Q., Horta, L. G., and Longman, R. W., “Identification of Observer/Kalman Filter Markov Parameters: Theory and Experiments,” *Journal of Guidance, Control, and Dynamics*, Vol. 16, No. 2, 1993, pp. 320–329.
 48. Flinois, T. L. B. and Morgans, A. S., “Feedback control of unstable flows: a direct modelling approach using the Eigensystem Realisation Algorithm,” *Journal of Fluid Mechanics*, Vol. 793, apr 2016, pp. 41–78.
 49. Schmid, P. J., “Dynamic mode decomposition of numerical and experimental data,” *Journal of fluid mechanics*, Vol. 656, 2010, pp. 5–28.

50. Rowley, C. W., Mezić, I., Bagheri, S., Schlatter, P., and Henningson, D. S., “Spectral analysis of nonlinear flows,” *J. Fluid Mech.*, Vol. 641, 2009.
51. Tu, J., Rowley, C., Luchtenberg, D., Brunton, S., and Kutz, J., “On dynamic mode decomposition: Theory and algorithms,” *Journal of Computational Dynamics*, 2014.
52. Proctor, J. L., Brunton, S. L., and Kutz, J. N., “Dynamic mode decomposition with control,” *SIAM Journal on Applied Dynamical Systems*, Vol. 15, No. 1, 2016, pp. 142–161.
53. Dawson, S., Hemati, M., Williams, M., and Rowley, C., “Characterizing and Correcting for the Effect of Sensor Noise in the Dynamic Mode Decomposition,” *Experiments in Fluids*, Vol. 57, No. 42, 2016.
54. Askham, T. and Kutz, J., “Variable Projection Methods for an Optimized Dynamic Mode Decomposition,” *SIAM Journal of Applied Dynamical Systems*, Vol. 17, No. 1, 2018, pp. 380–416.
55. Nonomura, T., Shibata, H., and Takaki, R., “Dynamic mode decomposition using a Kalman filter for parameter estimation,” *AIP Advances*, Vol. 8, No. 10, 2018.
56. Zhang, W. and Wei, M., “Model order reduction using DMD modes and adjoint DMD modes,” *AIAA Paper 2017-3482*, 2017.
57. Brogan, W. L., *Modern control theory*, Prentice-Hall Englewood Cliffs, NJ, 1974.
58. Hamdan, A. and Nayfeh, A., “Measures of modal controllability and observability for first-and second-order linear systems,” *Journal of guidance, control, and dynamics*, Vol. 12, No. 3, 1989, pp. 421–428.